

Cite this: *Anal. Methods*, 2025, 17, 8610

# Fluorescent/ratiometric colorimetric dual-node sensor based on Fe/N co-doped carbon dots for nitrite detection

Tiechun Li,<sup>a</sup> Mengjia Guo,<sup>b</sup> Weiwei Luo,<sup>a</sup> Quanping Diao,<sup>a</sup> Linlin Lv<sup>a</sup> and Pinyi Ma<sup>b</sup>

Nitrite ( $\text{NO}_2^-$ ) has been extensively utilized in the food industry as a preservative and colorant; however, excessive intake can lead to serious health issues, highlighting the need for accurate and efficient detection methods. In this work, blue fluorescent iron and nitrogen co-doped carbon dots (Fe/N-CDs) were synthesized *via* a one-step hydrothermal method using ferric chloride, ethylenediaminetetraacetic acid (EDTA), and diethylenetriamine (DETA) as precursors. The prepared Fe/N-CDs exhibited excellent peroxidase-like activity. By leveraging the catalytic activity of Fe/N-CDs and the oxidation and diazotization reactions induced by  $\text{NO}_2^-$ , we developed a dual-mode fluorescent and ratiometric colorimetric sensor for nitrite detection. The fluorescence and colorimetric methods had linear detection ranges of 2.5–75  $\mu\text{M}$  and 2.5–100  $\mu\text{M}$ , with detection limits of 0.68  $\mu\text{M}$  and 1.19  $\mu\text{M}$ , respectively. The developed dual-mode sensing platform was successfully applied to detect  $\text{NO}_2^-$  in both pickled vegetable and cured pork samples, demonstrating its feasibility in practical applications. Furthermore, the color of the reaction changed from blue to yellow as the  $\text{NO}_2^-$  concentration increased. Quantitative nitrite analysis was further achieved by capturing RGB values with smartphone-assisted color-recognition software, using the green-to-red (G/R) ratio as the analytical signal.

Received 9th September 2025  
Accepted 15th October 2025

DOI: 10.1039/d5ay01502b

[rsc.li/methods](https://rsc.li/methods)

## 1. Introduction

Nitrite ( $\text{NO}_2^-$ ) is widely used as a preservative and color-fixing agent in the food industry, primarily due to its ability to inhibit bacterial growth and enhance the color of meat products.<sup>1</sup> Additionally,  $\text{NO}_2^-$  can be generated naturally during the fermentation or storage of food products.<sup>2</sup> However, excessive intake of  $\text{NO}_2^-$  can pose significant health risks. Under acidic gastric conditions,  $\text{NO}_2^-$  can readily react with amides or secondary amines to produce highly carcinogenic *N*-nitrosamines, which increases the risk of cancers and gastrointestinal diseases.<sup>3</sup> Moreover, high concentrations of  $\text{NO}_2^-$  can oxidize hemoglobin to methemoglobin, and can in turn lead to tissue hypoxia manifested as symptoms such as dizziness and headaches.<sup>4,5</sup> For these reasons, the World Health Organization (WHO) has classified nitrite as a potential carcinogen. Many countries have implemented strict regulations to control and limit the use of  $\text{NO}_2^-$  in food products.<sup>6</sup> Therefore, it is critical to develop simple and accurate  $\text{NO}_2^-$  detection methods.

Various analytical methods have been developed for nitrite detection, including chromatography,<sup>7</sup> electrochemistry,<sup>8</sup> surface-enhanced Raman spectroscopy (SERS),<sup>9</sup> colorimetry,<sup>10</sup> and fluorescence-based methods.<sup>11</sup> Although chromatographic methods offer high accuracy, they rely on expensive instrumentation and require complex procedures. Electrochemical methods typically require elaborate electrode modifications and are limited by poor stability. In contrast, fluorescence and colorimetric methods have gained widespread attention due to their operational simplicity, high sensitivity, and visual interpretability. Furthermore, multimodal detection methods provide multiple signals that can mutually verify one another, which enhances the accuracy and reliability of the detection, particularly in complex sample matrices.<sup>12,13</sup> Thus, the development of multimodal  $\text{NO}_2^-$  detection is highly desirable.

Nanozymes are nanomaterials that exhibit enzyme-like catalytic activities. They are known for their high catalytic efficiency, low cost, and excellent stability.<sup>14</sup> To date, numerous nanozymes, including metal-organic frameworks,<sup>15</sup> metal oxides,<sup>16</sup> single-atom nanozymes,<sup>17</sup> and carbon-based nanozymes,<sup>18</sup> have been synthesized and applied in food safety monitoring, environmental analysis, and biosensing. Carbon-based nanozymes, such as carbon dots (CDs), graphene, and carbon nanotubes, have received considerable attention.<sup>19</sup> CDs, in particular, exhibit remarkable catalytic performance, tunable fluorescence, excellent stability, and high water solubility, in

<sup>a</sup>Liaoning Key Laboratory of Development and Utilization for Natural Products Active Molecules, School of Chemistry and Life Science, Anshan Normal University, Anshan, China. E-mail: [litiechun@asnc.edu.cn](mailto:litiechun@asnc.edu.cn)

<sup>b</sup>College of Chemistry, Jilin Province Research Center for Engineering and Technology of Spectral Analytical Instruments, Jilin University, Qianjin Street 2699, Changchun, 130012, China

addition to their simple preparation procedures and ease of functionalization.<sup>20,21</sup> For these reasons, they have been extensively employed in fluorescent sensing and bioimaging applications. Furthermore, heteroatom doping can significantly enhance the catalytic activity of CDs. Iron-doped carbon dots, in particular, have been widely investigated due to their low cost, high catalytic activity, and remarkable stability.<sup>22,23</sup> The combination of catalytic and fluorescent properties in CDs presents promising opportunities for multimodal analysis.<sup>24</sup> Currently, nanozyme-based  $\text{NO}_2^-$  detection methods utilize 3,3',5,5'-tetramethylbenzidine (TMB) as a chromogenic substrate, wherein nanozymes catalyze its oxidation to the blue-colored oxidized product ( $\text{TMB}^+$ ). This reaction, coupled with nitrite-induced oxidation and diazotization, enables the colorimetric detection of  $\text{NO}_2^-$ .<sup>25,26</sup> Nevertheless, only a few studies have reported the integration of the catalytic and fluorescent properties in nanozymes for dual-mode nitrite sensing.

In this work, iron and nitrogen co-doped carbon dots (Fe/N-CDs) emitting blue fluorescence were synthesized using a facile one-step hydrothermal method. The resulting Fe/N-CDs exhibited peroxidase-mimicking catalytic activity. By exploiting the catalytic activity of Fe/N-CDs and the nitrite-induced oxidation and diazotization reactions, we developed a fluorescent and ratiometric colorimetric dual-mode sensor for  $\text{NO}_2^-$  detection. Specifically, Fe/N-CDs catalyzed the oxidation of TMB by hydrogen peroxide ( $\text{H}_2\text{O}_2$ ), generating blue-colored  $\text{TMB}^+$  that exhibited a characteristic absorption peak at 652 nm. Upon the introduction of  $\text{NO}_2^-$ ,  $\text{TMB}^+$  was further oxidized and diazotized, resulting in the weakening of the absorption at 652 nm and the enhancement of the absorption at 445 nm. The ratio of these two signals allows for the quantitative colorimetric detection of  $\text{NO}_2^-$ . Furthermore, the di-electronic oxidation and diazotization products induced by  $\text{NO}_2^-$  effectively quenched the fluorescence of Fe/N-CDs through an inner filter effect (IFE), allowing for simultaneous fluorescence-based quantification of  $\text{NO}_2^-$ . The reaction system also exhibited a distinct color change visible to the naked eye, and RGB values obtained *via* smartphone-based color-recognition software (specifically, the G/R ratio) were employed as response signals for quantifying  $\text{NO}_2^-$ .

## 2. Experimental section

### 2.1 Chemicals and reagents

Ethylenediaminetetraacetic acid (EDTA), diethylenetriamine (DETA), 3,3',5,5'-tetramethylbenzidine (TMB), ascorbic acid (AA), glucose (Glu), glycine (Gly), serine (Ser), histidine (His), and 5.5'-dimethyl-1-pyrroline N-oxide (DMPO) were purchased from Aladdin Biochemical Technology Co., Ltd (Shanghai, China). Ferric chloride hexahydrate ( $\text{FeCl}_3 \cdot 6\text{H}_2\text{O}$ ), hydrogen peroxide ( $\text{H}_2\text{O}_2$ , 30%), sodium chloride (NaCl), potassium chloride (KCl), calcium chloride ( $\text{CaCl}_2$ ), magnesium chloride ( $\text{MgCl}_2$ ), sodium carbonate ( $\text{Na}_2\text{CO}_3$ ), aluminum nitrate ( $\text{Al}(\text{NO}_3)_3 \cdot 9\text{H}_2\text{O}$ ), and sodium sulfate ( $\text{Na}_2\text{SO}_4$ ) were purchased from Sinopharm Chemical Reagent Co., Ltd (Shanghai, China). Sodium nitrite ( $\text{NaNO}_2$ ) and dimethyl sulfoxide (DMSO) were purchased from Beijing Chemical Factory. All chemicals were of

analytical grade and used as received without further purification. Ultrapure water (18.2 M $\Omega$  cm) used throughout the experiments was obtained from a Millipore purification system.

### 2.2 Instrumentation

All spectroscopic and imaging measurements in this study were conducted using standard analytical instruments. Fluorescence spectra were recorded using an F-7000 fluorescence spectrophotometer (Hitachi, Japan), while UV-vis absorption spectra were measured with a Cary-60 UV-vis spectrophotometer (Agilent, USA). The morphology and microstructure of the synthesized Fe/N-CDs were characterized using a JEOL JEM-2100F transmission electron microscope (Hitachi, Japan). Surface chemical composition was analyzed by X-ray photoelectron spectroscopy (XPS) using an ESCALAB 250 instrument (Thermo Fisher Scientific, USA), and functional groups were identified by Fourier-transform infrared (FT-IR) spectroscopy with a Nicolet Avatar 360 spectrometer (Thermo Fisher Scientific, USA). Time-resolved fluorescence spectra were obtained with a FLS920 transient/steady-state spectrometer (Edinburgh Instruments, UK). Electron spin resonance (ESR) measurements were carried out using a Bruker E500 spectrometer (Bruker, Germany). The pH values of the solutions were measured with a PHS-3C pH meter (INESA Scientific Instrument Co., Ltd, China).

### 2.3 Synthesis of Fe/N-CDs

Fe/N-CDs were synthesized *via* a hydrothermal method, based on a previously reported procedure with slight modifications.<sup>27</sup> In a typical synthesis process,  $\text{FeCl}_3 \cdot 6\text{H}_2\text{O}$  (60 mg), EDTA (100 mg), and DETA (60  $\mu\text{L}$ ) were dissolved in 10 mL of ultrapure water under ultrasonic agitation for 30 min. The resulting solution was transferred into a 30 mL Teflon-lined stainless-steel autoclave and heated at 200 °C for 6 h. After the reaction was complete, the autoclave was allowed to cool naturally to room temperature, and the mixture was filtered through a 0.1  $\mu\text{m}$  microporous membrane. The filtrate containing Fe/N-CDs was collected and stored at 4 °C until subsequent experiments. Before use, the Fe/N-CDs solution was diluted 50-fold with ultrapure water.

### 2.4 Peroxidase-like activity and kinetic analysis of Fe/N-CDs

The peroxidase-like activity of Fe/N-CDs was assessed by mixing 4  $\mu\text{L}$  of TMB (10 mM), 10  $\mu\text{L}$  of  $\text{H}_2\text{O}_2$  (1 mM), and 45  $\mu\text{L}$  of Fe/N-CDs solution with 100  $\mu\text{L}$  of sodium acetate–acetic acid buffer solution (NaAc-HAc, 0.2 M, pH 4.0). The reaction mixture was incubated at 40 °C for 50 min, and the absorbance at 652 nm was recorded using a UV-vis spectrophotometer. Control experiments were conducted by mixing TMB with either Fe/N-CDs or  $\text{H}_2\text{O}_2$  to verify the catalytic activity of Fe/N-CDs.

Steady-state kinetic studies of Fe/N-CDs were carried out by varying concentrations of either TMB or  $\text{H}_2\text{O}_2$ . All kinetic experiments were conducted at 40 °C and pH 4.0. In one set of experiments, the concentrations of Fe/N-CDs and  $\text{H}_2\text{O}_2$  were kept constant, while the TMB concentration was varied. Absorbance at 652 nm was measured as a function of reaction time. In another set of experiments, the concentration of TMB

was fixed, while the  $\text{H}_2\text{O}_2$  concentration was varied. Kinetic parameters, including the maximum reaction velocity ( $v_{\text{max}}$ ) and the Michaelis–Menten constant ( $K_{\text{m}}$ ), were determined by fitting the experimental data to the Lineweaver–Burk double-reciprocal plot using the following equations:

$$v = \frac{v_{\text{max}}[\text{S}]}{K_{\text{m}} + [\text{S}]}$$

$$\frac{1}{v} = \frac{K_{\text{m}}}{v_{\text{max}}} \frac{1}{[\text{S}]} + \frac{1}{v_{\text{max}}}$$

where  $v$  is the initial reaction velocity and  $[\text{S}]$  is the substrate concentration (TMB or  $\text{H}_2\text{O}_2$ ).

### 2.5 Fluorescent and colorimetric detection of $\text{NO}_2^-$

Four microliters of TMB (10 mM), 10  $\mu\text{L}$  of  $\text{H}_2\text{O}_2$  (1 mM), and 45  $\mu\text{L}$  of Fe/N-CDs solution were mixed with 100  $\mu\text{L}$  of NaAc-HAc buffer (0.2 M, pH 4.0) and incubated at 40  $^\circ\text{C}$  for 50 min. After varying concentrations of  $\text{NO}_2^-$  were added, the final volume was adjusted to 400  $\mu\text{L}$  with ultrapure water. The mixture was further incubated at 40  $^\circ\text{C}$  for another 40 min, after which fluorescence and colorimetric measurements were performed. For fluorescence detection, emission spectra were recorded from 380 to 600 nm at an excitation wavelength of 360 nm. Quantitative analysis was performed based on the fluorescence intensity ratio at 453 nm in the presence ( $F$ ) and absence ( $F_0$ ) of  $\text{NO}_2^-$ . For colorimetric detection, UV-vis absorption spectra were acquired from 200 to 800 nm, and quantitative analysis was based on the ratio of absorbance at 652 nm and 445 nm ( $A_{652}/A_{445}$ ).

### 2.6 Smartphone-assisted RGB detection of $\text{NO}_2^-$

Images of the reaction solutions containing different concentrations of  $\text{NO}_2^-$  were captured using a smartphone camera (iPhone 16 Pro, Apple Inc., USA) under uniform ambient daylight conditions. To minimize background interference, the samples were photographed against a plain white background at a fixed distance of approximately 15 cm. RGB values were extracted using the Colorimeter App (iOS, Apple App Store) installed on the smartphone, and the average values were obtained from the selected regions of interest (ROI) at the center of each sample. A standard calibration curve, a plot of G/R ratio vs.  $\text{NO}_2^-$  concentration, was used in the quantitative analysis of nitrite concentrations.

### 2.7 Real sample analysis

Pickled vegetable and cured pork samples purchased from a local supermarket were analyzed using the standard addition method to evaluate the practical applicability of the sensor. Sample preparation was conducted following the Chinese National Standard (GB 5009.33-2016).<sup>28</sup> Processed samples were spiked with known concentrations of  $\text{NO}_2^-$  (10.00, 25.00, and 50.00  $\mu\text{M}$ ), and detection was performed as described in Section 2.5.

## 3. Results and discussion

### 3.1 Characterization of Fe/N-CDs

The morphology and size distribution of the synthesized Fe/N-CDs were investigated using transmission electron microscopy (TEM). As shown in Fig. 1A, Fe/N-CDs had uniform spherical shapes and good dispersion; their average particle diameter was approximately 2.3 nm. Well-defined lattice fringes were observed, indicating a high degree of crystallinity. Fourier-transform infrared (FT-IR) spectroscopy was employed to identify the surface functional groups of Fe/N-CDs. As shown in Fig. 1B, the broad absorption band at 3435  $\text{cm}^{-1}$  is attributed to the stretching vibrations of O–H and/or N–H groups, likely associated with hydrogen bonding. The peak at 3113  $\text{cm}^{-1}$  can be assigned to =C–H stretching vibrations of aromatic or olefinic structures. The band at 1630  $\text{cm}^{-1}$  can be ascribed to the stretching vibrations of C=O and/or C=N groups. Additionally, the peak at 1395  $\text{cm}^{-1}$  corresponds to C–N stretching vibrations, indicating the presence of nitrogen-containing functional groups.<sup>29</sup> Notably, no distinct Fe–O/N peaks were observed, likely due to the low iron doping level. The surface chemical composition and elemental states of Fe/N-CDs were characterized by X-ray photoelectron spectroscopy (XPS). The full XPS survey spectrum (Fig. 1C) shows distinct peaks corresponding to C 1s, N 1s, O 1s, and Fe 2p. The high-resolution C 1s spectrum (Fig. 1D) displays peaks at 284.8 eV, 285.7 eV, and 287.6 eV, which can be assigned to C–C, C–N, and C=O bonds, respectively.<sup>30</sup> The N 1s spectrum (Fig. 1E) shows peaks at 398.4 eV, 399.5 eV, and 400.9 eV, corresponding to pyridinic N, pyrrolic N, and graphitic N, respectively. Pyridinic and pyrrolic nitrogen are known to contribute to the formation of  $\pi$ -conjugated systems and facilitate the anchoring of Fe sites.<sup>31</sup> In the Fe 2p spectrum (Fig. 1F), the peaks at 709.7 eV and 713.4 eV are attributed to  $\text{Fe}^{2+}$  and  $\text{Fe}^{3+}$  (Fe 2p<sub>3/2</sub>), respectively, while those at 723.2 eV and 727.2 eV correspond to  $\text{Fe}^{2+}$  and  $\text{Fe}^{3+}$  (Fe 2p<sub>1/2</sub>), respectively.<sup>2</sup> These peaks indicate that Fe/N-CDs are present in both oxidation states. Collectively, these results confirm the successful synthesis and doping of Fe and N in the carbon dot framework.

### 3.2 Optical properties of Fe/N-CDs

The optical properties of Fe/N-CDs were characterized using UV-vis absorption and fluorescence spectroscopy. As shown in Fig. 2A, Fe/N-CDs exhibited a broad absorption band in the 200–400 nm region, with a peak at 240 nm attributed to the  $\pi$ – $\pi^*$  transition of  $\text{sp}^2$ -hybridized graphitic carbon domains.<sup>32</sup> The excitation-dependent photoluminescence behavior of Fe/N-CDs is illustrated in Fig. 2B. As the excitation wavelength was increased from 310 to 400 nm, the emission peak gradually redshifted from 442 to 467 nm, and the maximum fluorescence intensity was observed at an excitation wavelength of 360 nm, which is indicative of an excitation-dependent emission behavior. The fluorescence stability of Fe/N-CDs was systematically evaluated under various environmental conditions, including pH, ionic strength, and UV irradiation duration. As shown in Fig. 2C, the fluorescence intensity of Fe/N-CDs

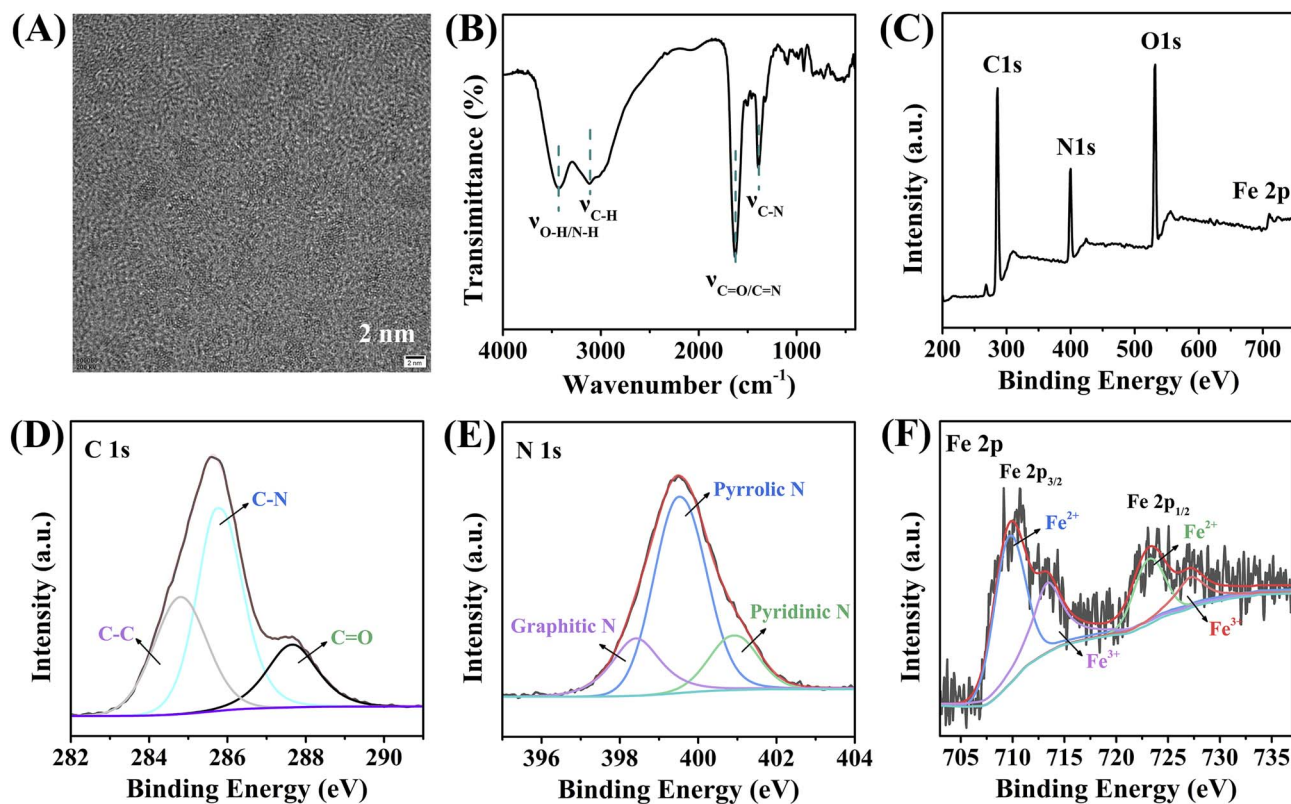


Fig. 1 (A) TEM image of Fe/N-CDs. (B) FT-IR spectrum of Fe/N-CDs. (C) XPS survey spectrum of Fe/N-CDs. (D-F) High-resolution XPS spectra of C 1s, N 1s, and Fe 2p.

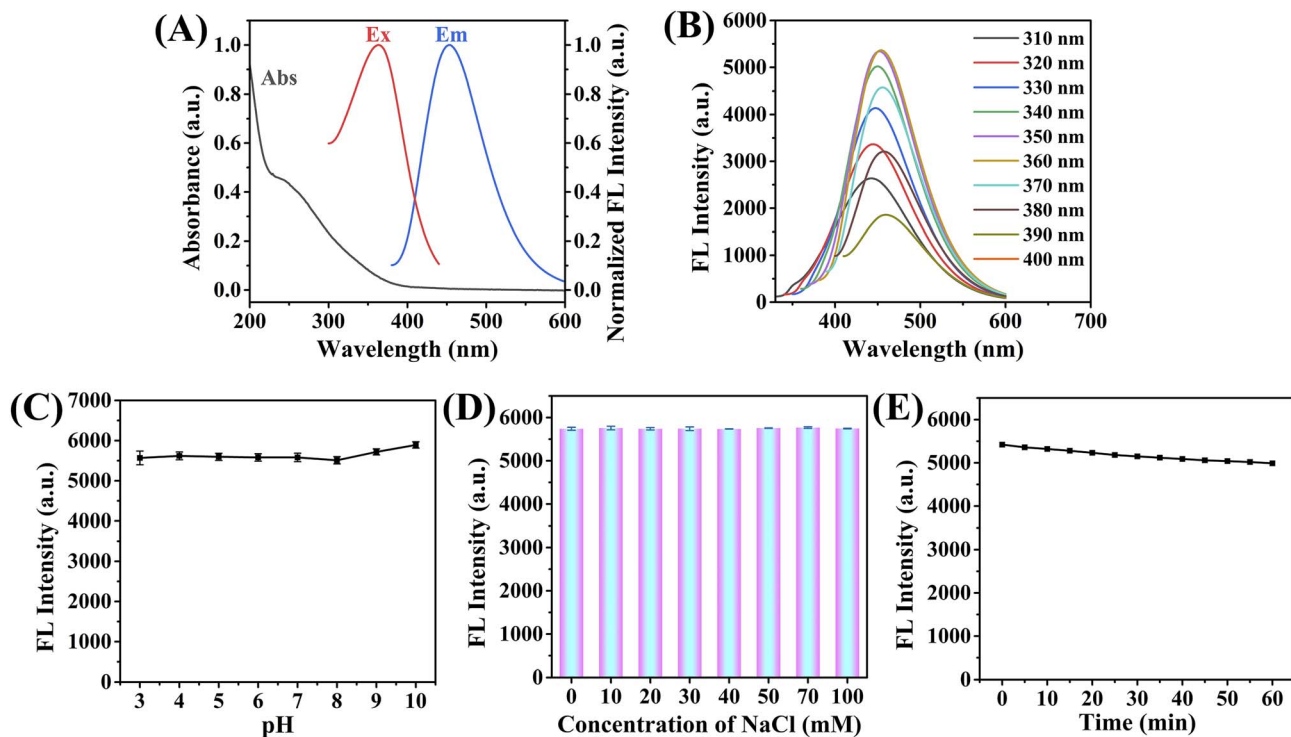


Fig. 2 (A) UV-vis absorption and fluorescence emission spectra of Fe/N-CDs. (B) Excitation-dependent fluorescence emission spectra of Fe/N-CDs. (C) Effect of pH on fluorescence intensity of Fe/N-CDs. (D) Effect of ionic strength (100 mM NaCl) on fluorescence intensity of Fe/N-CDs. (E) Effect of UV irradiation duration on fluorescence intensity of Fe/N-CDs. ( $\lambda_{\text{ex}} = 360$  nm).

remained relatively stable across a pH range of 3.0–8.0, indicating low sensitivity to pH changes. Moreover, Fe/N-CDs showed excellent resistance to high ionic strength, as they were able to maintain their fluorescence intensity in the presence of 100 mM NaCl (Fig. 2D). In addition, the photostability of Fe/N-CDs was evaluated by subjecting the samples to continuous UV irradiation for 60 min. As illustrated in Fig. 2E, the fluorescence intensity of over 90% of its original value was retained, confirming the excellent optical stability under prolonged illumination.

### 3.3 Peroxidase-like activity of Fe/N-CDs

The peroxidase-like catalytic activity of Fe/N-CDs was systematically evaluated using TMB as the chromogenic substrate. Peroxidase enzymes catalyze the oxidation of TMB by hydrogen peroxide ( $\text{H}_2\text{O}_2$ ), generating a blue-colored oxidized product ( $\text{TMB}^+$ ), which exhibits a characteristic absorption peak at 652 nm. As shown in Fig. 3A, a distinct absorbance peak at 652 nm appeared only when both  $\text{H}_2\text{O}_2$  and Fe/N-CDs were present, confirming the intrinsic peroxidase-mimicking activity of Fe/N-CDs. To further investigate the catalytic mechanism, electron spin resonance (ESR) spectroscopy was employed using 5,5-dimethyl-1-pyrroline N-oxide (DMPO) as a spin-trapping agent to trap hydroxyl radicals ( $\cdot\text{OH}$ ) in the solution. As illustrated in Fig. 3B, a characteristic ESR signal with an intensity ratio of 1 : 2 : 2 : 1 was observed in the presence of both Fe/N-CDs and  $\text{H}_2\text{O}_2$ . The signal corresponds to the DMPO- $\text{OH}$

adducts.<sup>33</sup> This result indicates that Fe/N-CDs can catalyze the decomposition of  $\text{H}_2\text{O}_2$  to generate  $\cdot\text{OH}$  radicals, which subsequently oxidize TMB. The influence of pH and temperature on the catalytic performance of Fe/N-CDs was also investigated. As shown in Fig. 3C, the catalytic activity of Fe/N-CDs was pH-dependent, with the maximum activity observed at pH 4.0 (acidic conditions). The catalytic activity decreased significantly as the pH was increased. Similarly, the catalytic activity increased with increasing temperature up to 40 °C, beyond which it declined (Fig. 3D). Therefore, pH 4.0 and 40 °C were selected as the optimal conditions for subsequent catalytic assays.

Under these optimal conditions, steady-state kinetic studies were conducted to evaluate the enzyme-like catalytic behavior of Fe/N-CDs toward TMB and  $\text{H}_2\text{O}_2$ . Michaelis–Menten curves and corresponding Lineweaver–Burk double-reciprocal plots were constructed and used to derive the kinetic parameters. With TMB as the substrate, the Michaelis constant ( $K_m$ ) and maximum reaction rate ( $v_{\text{max}}$ ) were calculated to be 0.070 mM and  $2.31 \times 10^{-8} \text{ M s}^{-1}$ , respectively (Fig. 3E). With  $\text{H}_2\text{O}_2$  as the substrate, the  $K_m$  and  $v_{\text{max}}$  values were determined to be 0.064 mM and  $4.72 \times 10^{-8} \text{ M s}^{-1}$ , respectively (Fig. 3F).  $K_m$  reflects substrate binding affinity with lower values indicating stronger affinity, while  $v_{\text{max}}$  reflects catalytic efficiency with higher values indicating higher catalytic performance.<sup>34</sup>

Table 1 shows a comparative summary of the catalytic parameters of Fe/N-CDs, natural horseradish peroxidase (HRP),

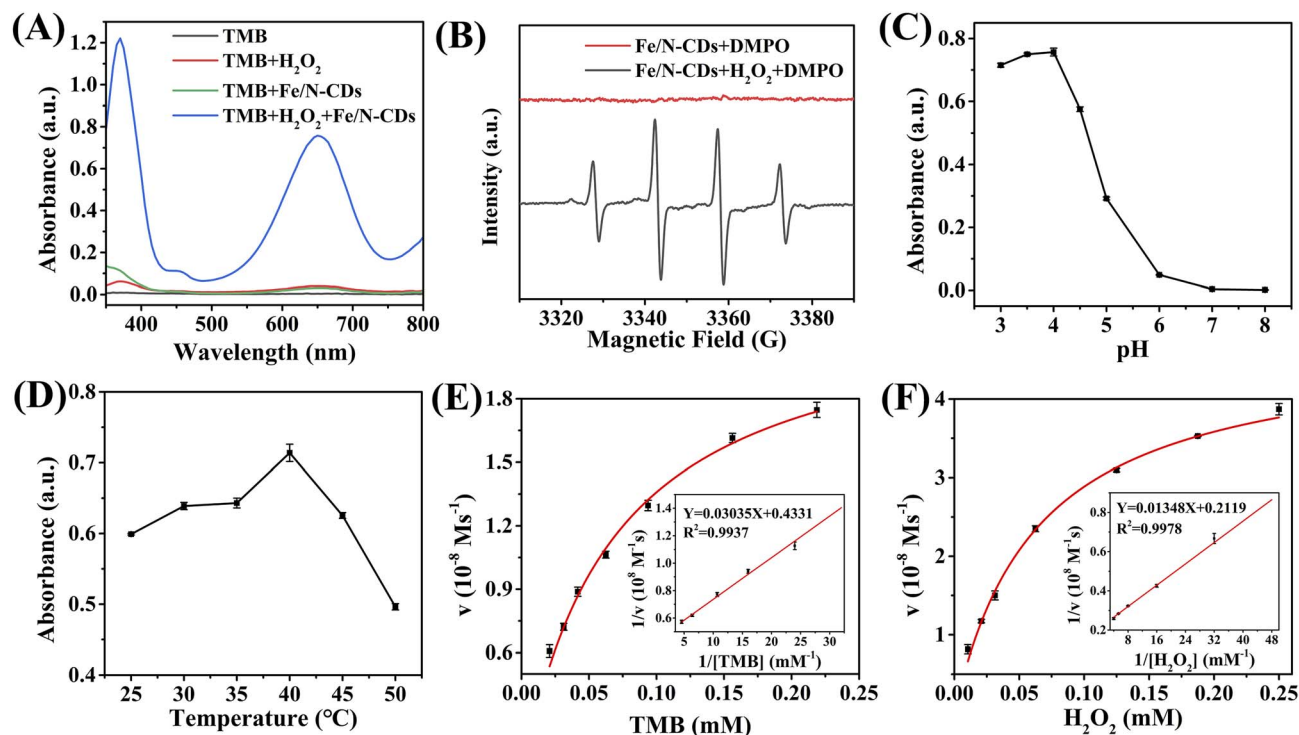


Fig. 3 (A) UV-vis absorption spectra of different reaction systems. (B) EPR spectra of various systems confirming  $\cdot\text{OH}$  generation. (C) Effect of pH on peroxidase-like activity of Fe/N-CDs. (D) Effect of temperature on peroxidase-like activity of Fe/N-CDs. (E) Steady-state kinetic curve constructed using TMB as the substrate as the substrate (inset: corresponding Lineweaver–Burk plot). (F) Steady-state kinetic constructed using  $\text{H}_2\text{O}_2$  as the substrate (inset: corresponding Lineweaver–Burk plot).

Table 1 Comparison of kinetic parameters of Fe/N-CDs with other catalysts

Catalysts	Substance	$K_m$ (mM)	$v_{max}$ ( $10^{-8}$ M s $^{-1}$ )	Catalytic efficiency ( $v_{max}/K_m$ , $10^{-5}$ s $^{-1}$ )	References
HRP	TMB	0.43	10.00	23.26	35
	H <sub>2</sub> O <sub>2</sub>	3.70	8.71	2.35	
Fe/ZnO	TMB	1.00	12	12.00	36
	H <sub>2</sub> O <sub>2</sub>	0.064	6.55	102.34	
Si-CoO	TMB	0.0589	25.0	424.45	37
	H <sub>2</sub> O <sub>2</sub>	0.023	1.04	45.22	
Ag-CQDs	TMB	0.0997	0.578	5.80	38
	H <sub>2</sub> O <sub>2</sub>	1.883	1.373	0.73	
N/S-CDs	TMB	0.0765	0.3096	4.05	39
	H <sub>2</sub> O <sub>2</sub>	0.0488	0.6799	13.92	
Fe/N-CDs	TMB	0.070	2.31	33.00	This work
	H <sub>2</sub> O <sub>2</sub>	0.064	4.72	73.75	

and other reported nanozymes. The data indicate that Fe/N-CDs had a lower  $K_m$  and higher  $v_{max}$  compared to many previously reported materials, which are indicative of their stronger substrate affinity and superior catalytic efficiency. In addition, the high-resolution XPS spectrum (Fig. 1F) revealed characteristic peaks of both Fe<sup>2+</sup> and Fe<sup>3+</sup>, suggesting that the peroxidase-like activity originates from the coexistence of Fe<sup>2+</sup>/Fe<sup>3+</sup> redox couples. These redox-active species can participate in a Fenton-like catalytic cycle, where Fe<sup>2+</sup> promotes the decomposition of H<sub>2</sub>O<sub>2</sub> to produce ·OH radicals, and Fe<sup>3+</sup> is subsequently reduced back to Fe<sup>2+</sup>, sustaining continuous catalytic turnover. This mechanism is consistent with the ESR results and provides a rational explanation for the observed activity.

Furthermore, to better substantiate the enzyme-like advantages, apparent catalytic efficiency values ( $v_{max}/K_m$ ) were calculated after converting  $K_m$  into molar units. The catalytic efficiency of Fe/N-CDs was determined to be  $33.0 \times 10^{-5}$  s $^{-1}$  for TMB and  $73.75 \times 10^{-5}$  s $^{-1}$  for H<sub>2</sub>O<sub>2</sub>, both of which are higher than those of HRP ( $23.26 \times 10^{-5}$  s $^{-1}$  and  $2.35 \times 10^{-5}$  s $^{-1}$ , respectively). These results indicate that Fe/N-CDs not only mimic natural peroxidase activity but also outperform HRP in substrate affinity and apparent catalytic efficiency, while maintaining advantages of stability and low cost. It should be noted that the kinetic parameters reported for different nanozymes are strongly influenced by the experimental conditions, such as pH and temperature, which vary across studies. Therefore, while the values summarized in Table 1 provide meaningful relative trends, they should not be interpreted as strictly standardized comparisons under identical conditions.

Collectively, these findings confirm that Fe/N-CDs possess excellent peroxidase-like activity mediated by Fe<sup>2+</sup>/Fe<sup>3+</sup> redox cycling and hold strong potential as catalytic nanomaterials for sensing applications.

### 3.4 Detection mechanism of the fluorescent/ratiometric colorimetric dual-mode sensor

A ratiometric colorimetric sensor for NO<sub>2</sub><sup>-</sup> detection was developed based on the catalytic oxidation of TMB by Fe/N-CDs in the presence of H<sub>2</sub>O<sub>2</sub> and the subsequent NO<sub>2</sub><sup>-</sup>-induced diazotization and oxidation reactions. As illustrated in Fig. 4A, Fe/N-CDs catalyze the oxidation of TMB by H<sub>2</sub>O<sub>2</sub>, generating

a blue-colored oxidation product (TMB<sup>+</sup>), which exhibits a characteristic absorption peak at 652 nm. Upon the addition of NO<sub>2</sub><sup>-</sup>, the absorbance at 652 nm gradually decreased, while a new absorption peak emerged at 445 nm, accompanied by a solution color change from blue to green. These opposing spectral changes is the foundation for ratiometric colorimetric detection of NO<sub>2</sub><sup>-</sup>. This observation is attributed to the strong oxidative nature of NO<sub>2</sub><sup>-</sup> under acidic conditions, which enables the further oxidation of the mono-electron oxidation product TMB<sup>+</sup>. In addition, under strong acidic conditions, NO<sub>2</sub><sup>-</sup> can undergo diazotization reactions with the aromatic primary amine groups of TMB<sup>+</sup>, forming diazonium intermediates (Fig. 4B). Both the di-electronic oxidation product and the diazonium derivative exhibited a strong absorption peak at 445 nm.

To confirm this mechanism, UV-vis spectra of different reaction systems were recorded. As shown in Fig. 4C, the addition of 200 μM ascorbic acid (AA) to the Fe/N-CDs + TMB + H<sub>2</sub>O<sub>2</sub> system resulted in complete loss of the absorption at 652 nm. In the Fe/N-CDs + TMB + H<sub>2</sub>O<sub>2</sub> + NO<sub>2</sub><sup>-</sup> system, the addition of AA caused the 652 nm peak to disappear and decreased the 445 nm peak intensity. Since AA can reduce the quinone-imine structure of TMB<sup>+</sup> to its aromatic amine but does not affect diazonium groups, these results suggest that in the presence of NO<sub>2</sub><sup>-</sup>, part of TMB<sup>+</sup> undergoes further oxidation while another part undergoes diazotization. To elucidate the fluorescence sensing mechanism, emission spectra of different systems were measured. As shown in Fig. 4D, the addition of NO<sub>2</sub><sup>-</sup>, H<sub>2</sub>O<sub>2</sub>, or TMB had negligible impacts on the fluorescence intensity of Fe/N-CDs. However, a significant decrease in fluorescence intensity was observed in the Fe/N-CDs + TMB + H<sub>2</sub>O<sub>2</sub> system, likely due to the broad absorption band of TMB<sup>+</sup> in the 350–600 nm range. Upon the addition of NO<sub>2</sub><sup>-</sup>, the fluorescence of Fe/N-CDs was further quenched, likely due to the presence of di-electronic oxidation and diazonium products. As shown in Fig. 4E, increasing NO<sub>2</sub><sup>-</sup> concentrations resulted in enhanced absorption at 445 nm and greater overlap between product absorption and Fe/N-CDs emission spectra. This suggests that the observed fluorescence quenching may be attributed to either the inner filter effect (IFE) or Förster resonance energy transfer (FRET). Notably, FRET typically reduces fluorescence

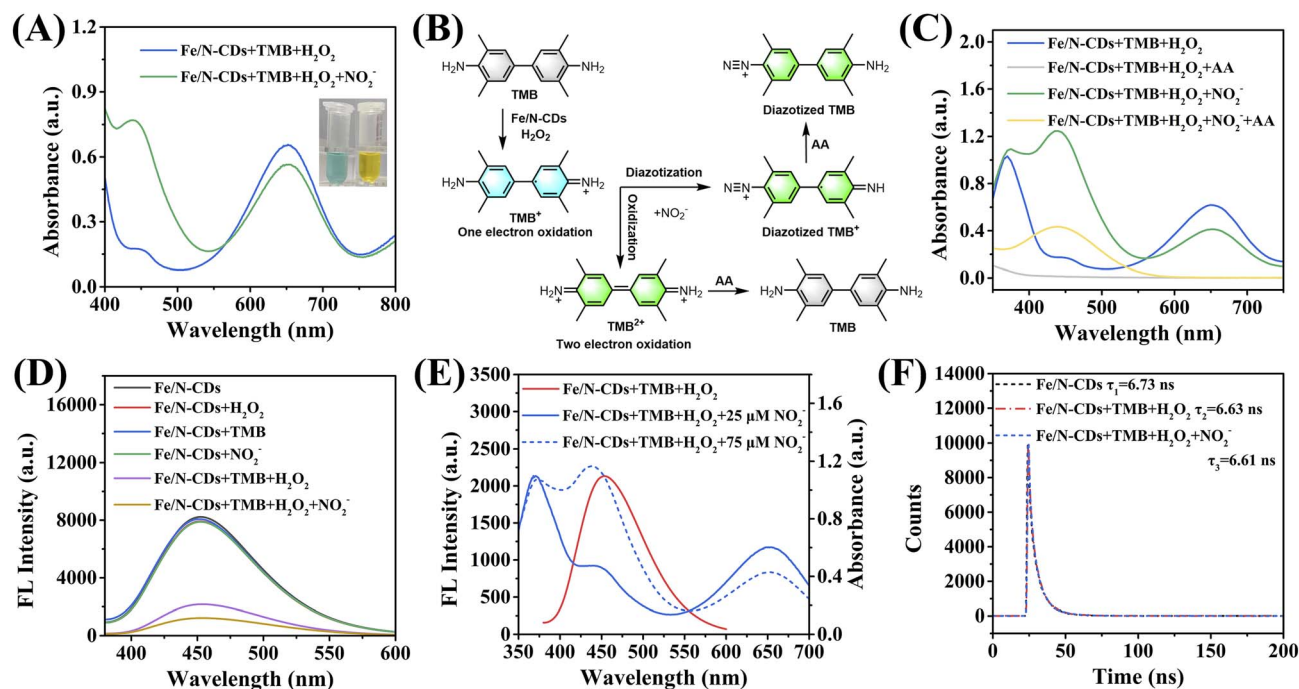


Fig. 4 (A) UV-vis absorption spectra of Fe/N-CDs + TMB + H<sub>2</sub>O<sub>2</sub> system and Fe/N-CDs + TMB + H<sub>2</sub>O<sub>2</sub> + NO<sub>2</sub><sup>-</sup> systems (inset: photographs of the solutions without (left) and with (right) NO<sub>2</sub><sup>-</sup>). (B) Proposed reaction mechanism of ratiometric colorimetric NO<sub>2</sub><sup>-</sup> detection. (C) Validation of the reaction mechanism. (D) Fluorescence emission spectra of different systems. (E) Fluorescence emission spectra of Fe/N-CDs + TMB + H<sub>2</sub>O<sub>2</sub> system and UV-vis absorption spectra of Fe/N-CDs + TMB + H<sub>2</sub>O<sub>2</sub> + NO<sub>2</sub><sup>-</sup> system. (F) Fluorescence decay curves of Fe/N-CDs, Fe/N-CDs + TMB + H<sub>2</sub>O<sub>2</sub>, and Fe/N-CDs + TMB + H<sub>2</sub>O<sub>2</sub> + NO<sub>2</sub><sup>-</sup> systems.

lifetime, while IFE does not.<sup>40</sup> To differentiate between these two quenching mechanisms, time-resolved fluorescence decay measurements were performed. As depicted in Fig. 4F, the fluorescence lifetimes of Fe/N-CDs in the Fe/N-CDs, Fe/N-CDs + TMB + H<sub>2</sub>O<sub>2</sub>, and Fe/N-CDs + TMB + H<sub>2</sub>O<sub>2</sub> + NO<sub>2</sub><sup>-</sup> systems remained essentially unchanged. This confirms that the observed fluorescence quenching is not due to FRET but rather results from IFE arising from the spectral overlap between product absorption and Fe/N-CDs emission. Therefore, the dual-mode sensor relies on the catalytic generation of TMB<sup>+</sup> and its NO<sub>2</sub><sup>-</sup>-mediated conversion into strongly absorbing products that trigger ratiometric absorbance changes and fluorescence quenching *via* the inner filter effect.

### 3.5 Performance evaluation for fluorescent and colorimetric detection of NO<sub>2</sub><sup>-</sup>

Given that the peroxidase-like activity of Fe/N-CDs was optimal at pH 4.0 and 40 °C, these conditions were employed for subsequent detection assays. To further optimize the sensor performance, the best reaction time for Fe/N-CDs-catalyzed oxidation of TMB and the subsequent TMB<sup>+</sup>-NO<sub>2</sub><sup>-</sup> reaction were determined. As shown in Fig. 5A, the absorbance at 652 nm reached a plateau after 50 min, indicating the completion of the catalytic oxidation step. In addition, the  $A_{652}/A_{445}$  ratio gradually decreased with increasing reaction time and stabilized after 40 min (Fig. 5B). Therefore, 50 min and 40 min were set as the optimal times for TMB oxidation and the subsequent TMB<sup>+</sup>-NO<sub>2</sub><sup>-</sup> reaction, respectively.

Under optimal conditions, the performance of the dual-mode sensor in quantitative detection of NO<sub>2</sub><sup>-</sup> was evaluated. As shown in Fig. 5C, the fluorescence intensity at 453 nm decreased progressively with increasing NO<sub>2</sub><sup>-</sup> concentration. A good linear relationship was observed between  $F/F_0$  and NO<sub>2</sub><sup>-</sup> concentration over the range of 2.5–75 μM (Fig. 5D), with a regression equation  $F/F_0 = -0.0070 [\text{NO}_2^-] + 0.9582$  ( $R^2 = 0.9940$ ). Using the formula  $3\delta/S$ , where  $\delta$  is the standard deviation of blank measurements and  $S$  is the slope of the calibration curve, the limit of detection (LOD) for fluorescence detection was calculated to be 0.68 μM.

In colorimetric detection, increasing NO<sub>2</sub><sup>-</sup> concentration resulted in a decrease in absorbance at 652 nm and a corresponding increase in absorbance at 445 nm (Fig. 5E). A ratiometric linear relationship between  $A_{652}/A_{445}$  and  $\log [\text{NO}_2^-]$  was observed over the range of 2.5–100 μM (Fig. 5F) and could be described by the equation  $A_{652}/A_{445} = -1.8289 \log([\text{NO}_2^-]) + 3.8647$  ( $R^2 = 0.9931$ ). The LOD for the ratiometric colorimetric method was determined to be 1.19 μM. A comparison between the present dual-mode sensing strategy and previously reported NO<sub>2</sub><sup>-</sup> detection methods is tabulated in Table 2. The proposed dual-mode sensing platform demonstrates superior analytical performance compared with many previously reported nitrite detection methods, with a wider linear range (2.5–100 μM) and lower detection limits (0.68 μM for fluorescence and 1.19 μM for colorimetry). These results substantiate the outstanding performance of Fe/N-CDs in nitrite detection. In addition, while the current system was optimized under mildly acidic

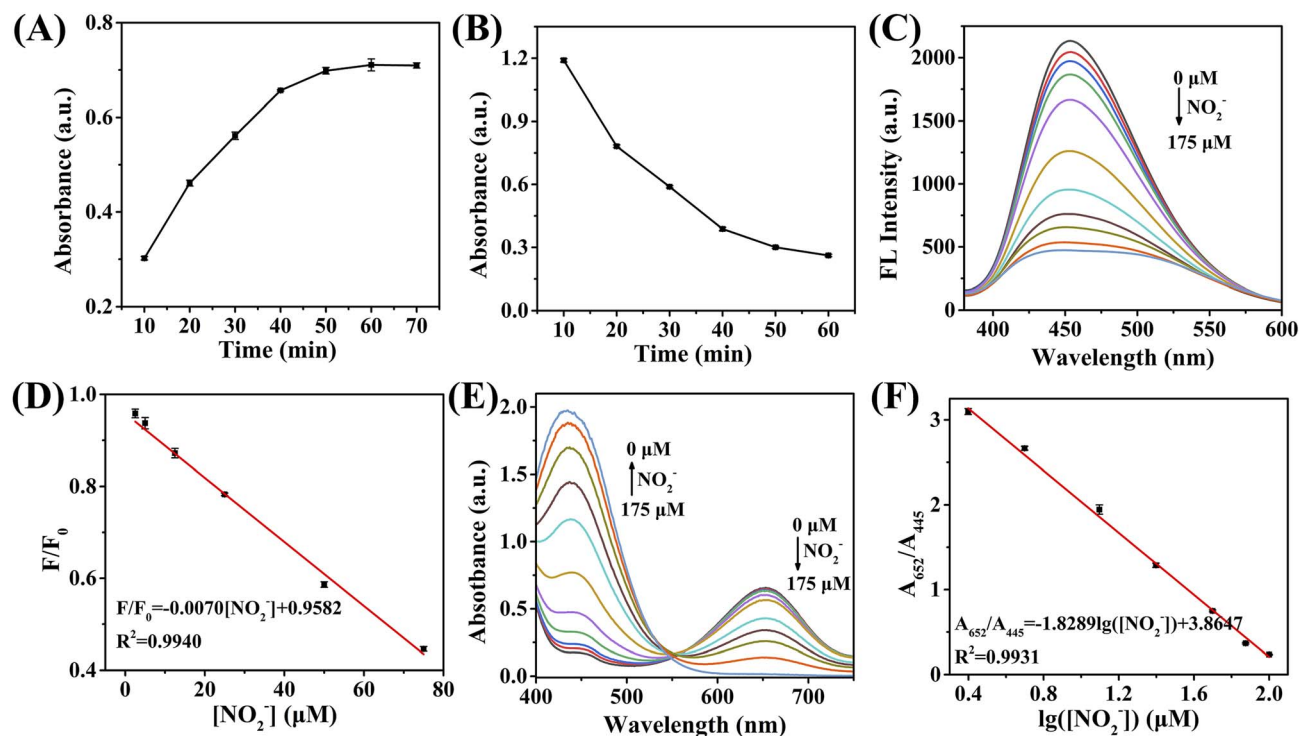


Fig. 5 (A) Optimization of reaction time for Fe/N-CDs-catalyzed TMB oxidation. (B) Optimization of reaction time for TMB<sup>+</sup>–NO<sub>2</sub><sup>–</sup> reaction. (C) Fluorescence emission spectra of the detection system in the presence of NO<sub>2</sub><sup>–</sup> at varying concentrations (0–175 μM). (D) Linear relationship between  $F/F_0$  and NO<sub>2</sub><sup>–</sup> concentration ( $F_0$  and  $F$  represent the fluorescence intensity before and after the addition of NO<sub>2</sub><sup>–</sup>, respectively). (E) UV-vis absorption spectra of the detection system in the presence of NO<sub>2</sub><sup>–</sup> at varying concentrations (0–175 μM). (F) Linear relationship between  $A_{652}/A_{445}$  and  $\lg[\text{NO}_2^-]$ .

Table 2 The performance comparison of the sensor with other methods for NO<sub>2</sub><sup>–</sup> detection

Methods	Materials	Linear range	LOD	References
Electrochemistry	ZrO <sub>2</sub> @MWCNTs	5–100 μM	0.94 μM	41
Electrochemistry	CTAB-SF5	30–500 μM	6.91 μM	42
SERS	GNP	1–100 μM	1 μM	43
Colorimetry	Mn-MOF	5–45 μM	0.15 μM	44
Colorimetry	AuNRs	8–100 μM	1.3 μM	45
Fluorometry	Tb-MOF	1–90 μM	0.75 μM	46
Fluorometry	BSA/MPA-AuNCs	5–30 μM	0.7 μM	47
Fluorometry	Fe/N-CDs	2.5–75 μM	0.68 μM	This work
Colorimetry		2.5–100 μM	1.19 μM	

conditions (pH 4.0), which is consistent with the reaction requirements of TMB oxidation and nitrite diazotization, such conditions are relevant to real-world acidic food matrices (*e.g.*, pickled vegetables). This confirms that the sensing platform is not only analytically advantageous but also practically applicable in food safety analysis.

The selectivity and anti-interference capability of the dual-mode sensor were assessed by evaluating the effects of common inorganic ions, glucose, and amino acids on its fluorescence and colorimetric signals. As shown in Fig. 6A and B, each of these potential interferents had negligible impacts on the fluorescence and absorbance signals. Moreover, the responses of the system to NO<sub>2</sub><sup>–</sup> in the presence of these interferents were nearly identical to those observed for NO<sub>2</sub><sup>–</sup>

alone. These results demonstrate that the dual-mode sensor possesses excellent selectivity and strong anti-interference capacity, making it suitable for nitrite detection in complex sample matrices.

### 3.6 Smartphone-assisted RGB analysis

As shown in Fig. 6C, the color of the reaction solution noticeably changed from blue to green and ultimately to yellow as the NO<sub>2</sub><sup>–</sup> concentration increased. This visible color shift allows for semi-quantitative detection of NO<sub>2</sub><sup>–</sup> by the naked eye. For more precise quantification, a smartphone was used to capture images of the solutions, and RGB values were extracted using a color recognition application. The results revealed a strong

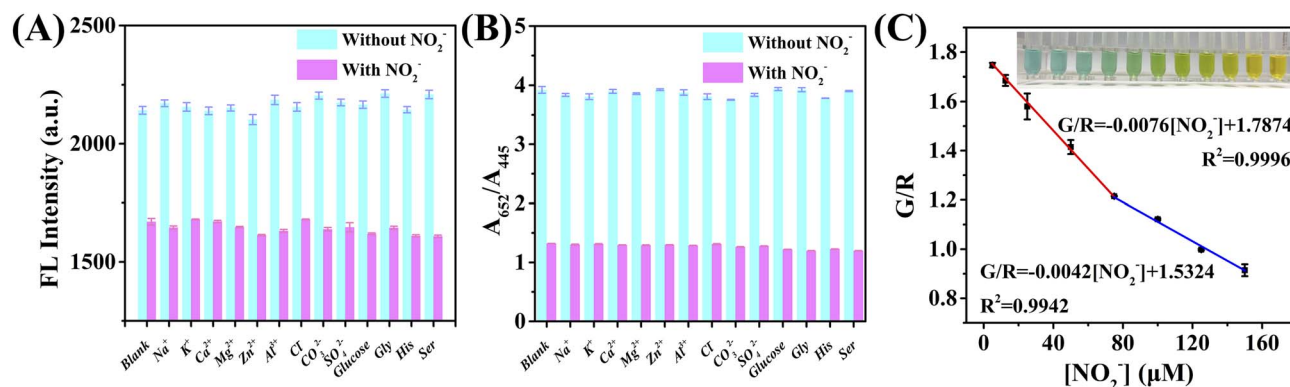


Fig. 6 Selectivity and anti-interference performance of the dual-mode sensor (interferent concentration: 100  $\mu\text{M}$  each): (A) fluorescence response and (B) colorimetric response. (C) Linear relationship between G/R and  $\text{NO}_2^-$  concentration (Inset: Photograph of the colorimetric sensing system in the presence of  $\text{NO}_2^-$  at increasing concentrations from left to right: 0, 2.5, 5, 12.5, 25, 50, 75, 100, 125, 150, and 175  $\mu\text{M}$ ).

linear relationship between the G/R value and  $\text{NO}_2^-$  concentration over two ranges: 5–75  $\mu\text{M}$  and 75–150  $\mu\text{M}$ . The corresponding regression equations were  $G/R = -0.0076 [\text{NO}_2^-] + 1.7874$  ( $R^2 = 0.9996$ ) and  $G/R = -0.0042 [\text{NO}_2^-] + 1.5324$  ( $R^2 = 0.9942$ ), respectively. Owing to its powerful data acquisition and processing capabilities, along with its user-friendly operation, the smartphone-based platform effectively overcomes the limitations of conventional analytical instrumentation. This approach is a convenient, accessible, and cost-effective alternative for on-site nitrite detection.

### 3.7 Real sample analysis

To assess the practical applicability of the dual-mode fluorescent/ratiometric colorimetric sensor, pickled vegetables and cured pork were used as representative real food samples. According to the National Food Safety Standard of China (GB 2762-2022), the maximum allowable concentration of nitrite in pickled vegetables is 20  $\text{mg kg}^{-1}$ .<sup>48</sup> The detection limit of the proposed sensor is significantly lower than this regulatory

threshold. Using the standard national method (GB 5009.33-2016), the  $\text{NO}_2^-$  content in untreated pickled vegetable samples was determined to be 0.36  $\mu\text{M}$ , while that in untreated cured pork samples was measured to be approximately 17.5  $\mu\text{M}$ . Importantly, the results obtained by both the fluorescence and colorimetric methods for these blank (untreated) samples were in good agreement with those measured by the GB 5009.33-2016 standard method, confirming the accuracy and reliability of our sensor. To further evaluate the accuracy of the sensor, recovery experiments were conducted using the standard addition method. As summarized in Table 3, the recovery rates obtained using the proposed fluorescence and colorimetric methods ranged from 100.1% to 102.5% for pickled vegetables and from 99.6% to 101.3% for cured pork, with relative standard deviations (RSDs) below 5.56% for both approaches. These results demonstrate that the developed sensor can accurately and reliably detect  $\text{NO}_2^-$  in both vegetable- and meat-based food matrices, confirming its practical applicability in food safety analysis.

Table 3 Detection of  $\text{NO}_2^-$  in actual and spiked food samples ( $n = 3$ )

Sample type	Detection mode	Spiked ( $\mu\text{M}$ )	Found ( $\mu\text{M}$ )	Recovery (%)	RSD (%)
Pickled vegetables	Fluorometry	0.00	0.36 $\pm$ 0.02	—	5.56
		10.00	10.38 $\pm$ 0.40	100.2	3.85
		25.00	25.87 $\pm$ 0.58	102.0	2.24
		50.00	50.42 $\pm$ 0.84	100.1	1.67
	Colorimetry	0.00	0.36 $\pm$ 0.01	—	2.78
		10.00	10.48 $\pm$ 0.09	101.2	0.86
		25.00	26.98 $\pm$ 0.32	102.5	1.23
		50.00	50.93 $\pm$ 0.52	101.1	1.02
Cured pork	Fluorometry	0.00	17.50 $\pm$ 0.35	—	2.00
		10.00	27.48 $\pm$ 0.62	99.8	2.26
		25.00	42.83 $\pm$ 0.74	101.3	1.73
		50.00	67.96 $\pm$ 1.12	100.9	1.65
	Colorimetry	0.00	17.50 $\pm$ 0.28	—	1.6
		10.00	27.63 $\pm$ 0.41	101.3	1.48
		25.00	42.62 $\pm$ 0.65	100.5	1.52
		50.00	67.31 $\pm$ 1.02	99.6	1.51

## 4. Conclusion

In this work, a dual-mode fluorescent/ratiometric colorimetric sensing strategy for  $\text{NO}_2^-$  detection was developed by integrating the peroxidase-like catalytic activity of Fe/N-CDs with the  $\text{NO}_2^-$ -induced oxidation and diazotization reactions, using TMB as the chromogenic substrate. The proposed methods had excellent analytical performance: the fluorescence method showed a linear detection range of 2.5–75  $\mu\text{M}$  with a detection limit of 0.68  $\mu\text{M}$ , whereas the colorimetric method had a linear range of 2.5–100  $\mu\text{M}$  and a detection limit of 1.19  $\mu\text{M}$ . The dual-mode output allows for mutual validation of results, thereby enhancing the reliability of detection. This sensing platform offers several advantages, including simple operation, high selectivity, strong anti-interference capability, and good sensitivity. It was successfully employed to detect  $\text{NO}_2^-$  in spiked pickled vegetable and cured pork samples, which demonstrates its applicability in real food analysis. Moreover, the system exhibited distinct multicolor changes in response to varying  $\text{NO}_2^-$  concentrations, allowing for semi-quantitative visual analysis. When combined with smartphone-based color recognition software, quantitative detection could be achieved based on RGB signals, offering a convenient and user-friendly approach for  $\text{NO}_2^-$  analysis. Overall, this dual-mode sensor has promising potential in food safety monitoring and represents a new strategy for the efficient  $\text{NO}_2^-$  detection.

## Author contributions

Tiechun Li: project administration, conceptualization, investigation, validation, writing – original draft, resources, supervision. Mengjia Guo: data curation, software, formal analysis. Weiwei Luo: validation, data curation, funding acquisition. Quanping Diao: visualization, data curation. Linlin Lv: formal analysis, writing – review & editing. Pinyi Ma: methodology, writing – review & editing.

## Conflicts of interest

The authors declare that they have no known competing financial interests or personal relationships that could have appeared to influence the work reported in this paper.

## Data availability

The data supporting this article have been included in the article.

## Acknowledgements

This work was supported by the PhD Initiation Fund of the Liaoning Science and Technology Department (Grant no. 2024-BS-282).

## References

- W. Wang, Q. Cai, C. Dai, J. Li, H. Xu, W. Zhang, Y. Chen and J. Hu, *Food Chem.*, 2025, **473**, 143126.
- W. Zuo, P. Wu, W. He, Q. Xiao, J. Yang, X. Liu, H. Jiang, J. Dai and Y. Ju, *Sens. Actuators, B*, 2023, **374**, 132816.
- X. Wang, Y. Guo, L. Zhao, Y. Yang, P. Wei and T. Yi, *J. Hazard. Mater.*, 2024, **478**, 135495.
- L. Zeng, Y. Ke, X. Yang, M. Lan, S. Zhao and B. Zhu, *Food Chem.*, 2024, **438**, 138044.
- Y. Chen, S. Li, R. Gao, Y. Shi, Y. Sun, G. I. N. Waterhouse and Z. Xu, *Food Chem.*, 2025, **473**, 143030.
- M. Yu, H. Zhang, Y. Liu, Y. Zhang, M. Shang, L. Wang, Y. Zhuang and X. Lv, *Food Chem.*, 2022, **374**, 131768.
- A. Antczak-Chrobot, P. Bak and M. Wojtczak, *Food Chem.*, 2018, **240**, 648–654.
- R. Feng, Y. Fan, Y. Fang and Y. Xia, *Molecules*, 2023, **28**, 4934.
- H. Yang, Y. Xiang, X. Guo, Y. Wu, Y. Wen and H. Yang, *Sens. Actuators, B*, 2018, **271**, 118–121.
- M. Sepahvand, F. Ghasemi and H. M. S. Hosseini, *Food Chem. Toxicol.*, 2021, **149**, 112025.
- W. Li, Y. Shi, X. Hu, Z. Li, X. Huang, M. Holmes, Y. Gong, J. Shi and X. Zou, *Food Control*, 2019, **106**, 106704.
- Z. Fu, L. Yang, Z. Ding and J. Xie, *Nanoscale*, 2025, **17**, 5328–5340.
- X. Luo, G. Huang, C. Bai, C. Wang, Y. Yu, Y. Tan, C. Tang, J. Kong, J. Huang and Z. Li, *J. Hazard. Mater.*, 2023, **443**, 130277.
- M. L. Mekonnen, E. M. Abda, A. Csaki and W. Fritzsche, *Anal. Chim. Acta*, 2025, **1337**, 343333.
- F. Wang, L. Chen, D. Liu, W. Ma, P. Dramou and H. He, *TRAC, Trends Anal. Chem.*, 2020, **133**, 116080.
- J. Matysik, O. Dlugosz and M. Banach, *J. Phys. Chem. B*, 2024, **128**, 8007–8016.
- H. Zhang, S. Zhang and Z. Zhang, *Chemosensors*, 2024, **12**, 209.
- H. Ding, B. Hu, B. Zhang, H. Zhang, X. Yan, G. Nie and M. Liang, *Nano Res.*, 2021, **14**, 570–583.
- D. Ofelia Lopez-Cantu, R. Berenice Gonzalez-Gonzalez, E. M. Melchor-Martinez, S. A. Hernandez Martinez, R. G. Araujo, L. Parra-Arroyo, J. Eduardo Sosa-Hernandez, R. Parra-Saldivar and H. M. N. Iqbal, *Int. J. Biol. Macromol.*, 2022, **194**, 676–687.
- M. Xie, F. Li, Y. Li, K. Qian, Y. Liang, B. Lei, Y. Liu, J. Cui and Y. Xiao, *Chem. Eng. J.*, 2025, **506**, 159956.
- J. Jin, L. Li, L. Zhang, Z. Luan, S. Xin and K. Song, *Front. Chem.*, 2021, **9**, 748044.
- M. Yang, J. Yao, B. Su, N. Xin, T. Zhou, M. Zeng, C. Wu, D. Wei, J. Sun and H. Fan, *J. Mater. Chem. B*, 2023, **11**, 5898–5909.
- R. Zhang, L. Liu, W. Li, X. Luo and F. Wu, *Colloids Surf., B*, 2023, **222**, 113125.
- H. Wei, H. Li, Y. Zhang, X. Wang, Z. Li, M. Zhou, Y. Lei, P. Guo, J. Liu and S. Yang, *Microchem. J.*, 2025, **208**, 112597.
- J. Zhang, H. Chen, J. Liu, J. Gui, M. Liu, Y. Zhang and S. Yao, *Talanta*, 2023, **258**, 124458.

- 26 X. Yue, L. Fu, C. Wu, C. Hao and Y. Bai, *J. Food Compos. Anal.*, 2025, **139**, 107027.
- 27 W. Zhang, Y. Wu, X. Liu, Y. Liu, Y. Zhang, W. Wang, X. Mu, R. Su, Y. Sun, D. Song and X. Wang, *Spectrochim. Acta, Part A*, 2022, **272**, 121003.
- 28 G. Wang, N. Feng, S. Zhao, L. Song, Y. Zhang, J. Tong, Y. Liu, X. Kang, T. Hu, I. A. Khan, K. Lu, H. Wu and J. Xie, *Food Chem.*, 2024, **434**, 137422.
- 29 Z. Ye, M. Ma, Y. Chen, J. Yang, C. Zhao, Q. Diao, P. Ma and D. Song, *Anal. Chem.*, 2024, **96**, 17984–17992.
- 30 Y. Long, J. Zhao, W. Ma, C. He, W. Pei, J. Hou, C. Hou and D. Huo, *Anal. Chem.*, 2024, **96**, 4774–4782.
- 31 X. Li, S. Ding, Z. Lyu, P. Tieu, M. Wang, Z. Feng, X. Pan, Y. Zhou, X. Niu, D. Du, W. Zhu and Y. Lin, *Small*, 2022, **18**, 2203001.
- 32 Q. Li, H. Lu, X. Wang, Z. Hong, Z. Fu, X. Liu and J. Zhou, *Chem. Eng. J.*, 2022, **443**, 136473.
- 33 X. Zhou, L. Li, Y. Wang, T. Kong, Z. Cao, H. Xie, W. Liang, Y. Wang, S. Qian, J. Chao and J. Zheng, *Anal. Chem.*, 2023, **95**, 8906–8913.
- 34 C. Yue, Y. Liu, M. Shi, T. Liu, C. Zhang and Y. Xian, *Microchem. J.*, 2025, **210**, 112837.
- 35 C. Xu, J. Xie, L. Yu, B. Shu, X. Liu, S. Chen, Q. Li, S. Qi and S. Zhao, *Food Chem.*, 2024, **454**, 139757.
- 36 X. Zou, Q. Chen, Q. Liu, X. Huang, Y. Tong and Z. Gong, *Microchem. J.*, 2025, **208**, 112314.
- 37 C. Jin, J. Lian, Y. Gao, K. Guo, K. Wu, L. Gao, X. Zhang, X. Zhang and Q. Liu, *ACS Sustainable Chem. Eng.*, 2019, **7**, 13989–13998.
- 38 W. Tan, G. Yao, H. Yu, Y. He, M. Lu, T. Zou, X. Li, P. Yin, P. Na, W. Yang, M. Yang and H. Wang, *Food Chem.*, 2024, **447**, 139020.
- 39 M. Tang, B. Zhu, Y. Wang, H. Wu, F. Chai, F. Qu and Z. Su, *Microchim. Acta*, 2019, **186**, 604.
- 40 X. Ye, D. Gao, X. Mu, Q. Wu, P. Ma and D. Song, *Anal. Chem.*, 2023, **95**, 4653–4661.
- 41 N. Rajab, H. Ibrahim, R. Y. A. Hassan and A. F. A. Youssef, *RSC Adv.*, 2023, **13**, 21259–21270.
- 42 H. Liu, H. Sun, P. Zhao, K. Shang, M. Fang, X. Tan, L. Yu and B. Ma, *Mater. Res. Bull.*, 2025, **186**, 113344.
- 43 C. Zhao, R. Shi, J. Wu, X. Luo and X. Liu, *Biosensors*, 2021, **11**, 223.
- 44 S. S. M. Ameen and K. M. Omer, *Food Chem.*, 2025, **462**, 141027.
- 45 M. Sepahvand, F. Ghasemi and H. M. S. Hosseini, *Anal. Methods*, 2021, **13**, 4370–4378.
- 46 H.-M. Wang, X.-N. Fang, Y. Xia and X.-B. Yin, *ACS Food Sci. Technol.*, 2022, **2**, 1911–1920.
- 47 H.-H. Deng, K.-Y. Huang, M.-J. Zhang, Z.-Y. Zou, Y.-Y. Xu, H.-P. Peng, W. Chen and G.-L. Hong, *Food Chem.*, 2020, **317**, 126456.
- 48 S. Liu, H. Qu, L. Yao, Y. Mao, L. Yan, B. Dong and L. Zheng, *Sens. Actuators, B*, 2023, **397**, 134707.